Rare Metal Materials and Engineering
Volume 55, Issue 7, July 2026
Available online at www.rmme.ac.cn

Science Press

Cite this article as: Jia Dongxiao, Zhao Pengfei, Liang Tian, et al. Effects of Gd on Microstructure and Mechanical Properties of Duplex Stainless Steels for Neutron Absorbing[J]. Rare Metal Materials and Engineering, 2026, 55(07): 1632-1640. DOI: https://doi.org/10.12442/j.issn.1002-185X.20250353.

ARTICLE

Effects of Gd on Microstructure and Mechanical Properties of Duplex Stainless Steels for Neutron Absorbing

Jia Dongxiao[1,2,3], Zhao Pengfei[1,2,3], Liang Tian[1,2,3], Hou Kunlei[1,2,3], Jiang Yuefeng[1,2,3], Ma Yingche[1,2,3]

[1] Shi-Changxu Innovation Center for Advanced Materials, Institute of Metal Research, Chinese Academy of Sciences, Shenyang 110016, China; [2] School of Materials Science and Engineering, University of Science and Technology of China, Shenyang 110016, China; [3] CAS Key Laboratory of Nuclear Materials and Safety Assessment, Institute of Metal Research, Chinese Academy of Sciences, Shenyang 110016, China

Abstract: The effects of different Gd contents on microstructure and mechanical properties of 00Cr23Ni8Mo1.4Mn1.4Si0.5 alloy were researched. Results indicate that element Gd exists mainly in three forms in the alloy: Gd_2O_3, $M_{12}Gd$, and M_3Gd phases (M=Fe, Cr, Ni). With the increase in Gd content, the contents of Gd-containing precipitate and ferrite phase are increased, whereas the austenite phase content is decreased. The Gd oxide and precipitation of two Gd-containing phases are the main causes of cracking in the alloy during the hot deformation process. The partially aggregated Gd oxide particles and the difficult-to-deform Gd-containing precipitates on the grain boundary jointly decrease the hot ductility of the alloy. With the increase in amount of Gd addition, the tensile strength and section shrinkage ratio of the alloy are decreased. Furthermore, M_3Gd is harder and more brittle, compared with $M_{12}Gd$, resulting in a more detrimental impact on the mechanical properties of alloy.

Key words: integration of structure and function; Gd; duplex stainless steel; neutron absorbing material; mechanical properties

1 Introduction

Nuclear energy is considered as a promising and strategic energy source for the future due to its safety, cleanliness, and abundant resources. However, spent nuclear fuel (SNF), which is inevitably generated in the nuclear power plant, releases a large number of thermal neutrons. For safe storage of SNF and neutron criticality control, high-performance neutron-absorbing structural materials are essential for SNF containers, racks, and transport parts[1–4].

Currently, borated austenitic stainless steels are widely used in the nuclear industry across various application scenarios due to their high strength, excellent corrosion resistance, and superior neutron absorptivity of the element boron[5–7]. However, the shortage of boron-containing materials is evident: the solubility of boron is limited in stainless steel, leading to the production of alloys containing less than 2.25wt% boron[8]. With the increase in volume fraction of boron-containing second phase, the plasticity of borated stainless steel is decreased[9]. Furthermore, the borides within borated stainless steel tend to form helium bubbles upon neutron absorption, leading to the degradation of shielding materials over extended storage periods[10].

Compared with boron, gadolinium (Gd) possesses a better neutron-absorbing ability[11]. The thermal neutron absorption cross-section of Gd (4.880×10^{-24} m^2) was approximately 13 times larger than that of ^{10}B (3.837×10^{-25} m^2)[7,12]. This property enables superior neutron-shielding rates and enhanced material properties with less Gd content. Moreover, after the capture reaction between Gd and thermal neutrons, Gd will not produce the bubbles or Li atoms like B, which will destroy the structural stability of the material[13–14]. In the simulated spent fuel pool environment, the Gd-containing phase in the alloy will not dissolve as quickly as the chromium boride in boron-containing steel, and it has better corrosion resistance[15]. Substituting Gd for B in the production of

Received date: July 03, 2025
Foundation item: Ling-Chuang Research Project of China National Nuclear Corporation (CNNC-LCKY-202279)
Corresponding author: Liang Tian, Ph. D., Associate Professor, Shi-Changxu Innovation Center for Advanced Materials, Institute of Metal Research, Chinese Academy of Sciences, Shenyang 110016, P. R. China, E-mail: tliang@imr. ac. cn; Ma Yingche, Ph. D., Professor, Shi-Changxu Innovation Center for Advanced Materials, Institute of Metal Research, Chinese Academy of Sciences, Shenyang 110016, P. R. China, E-mail: ycma@imr.ac.cn

thermal-neutron-absorbing materials presents a solution to the content-performance dilemma.

Although Gd has a much higher neutron-absorption capacity, studies of Gd-containing stainless steel are rare. Gd has extremely limited solubility in the austenitic or ferritic matrix, and thus it typically exists as Gd-containing precipitates[16–18]. Lo et al[19] found that the Gd-containing precipitate at the grain boundary restricts the hot workability of the material. During the hot processing of 316L stainless steel alloy with Gd, the presence of Gd phase seriously deteriorates the thermal ductility of the alloy, leading to cracking during the hot rolling process. It was found that the Gd-containing precipitates seriously reduce the cold and hot workability of the alloy, and the precipitation of $(Fe, Ni, Cr)_3Gd$ leads to Ni-poor and Cr-rich regions in the matrix, which deteriorates the stability of the matrix structure[20]. The low melting temperature of Gd results in a narrow temperature window for the hot processing of alloys, which leads to inferior thermal ductility during hot deformation and deteriorates the hot processing performance of alloy[21–22]. Choi et al[23] believed that the Gd-containing duplex stainless steel (DSS) has greater advantages than the austenitic stainless-steel matrix, because DSS has higher strength and better corrosion resistance than the single-phase austenitic stainless steels[24]. A 6 mm-thick, crack-free DSS plate containing 1wt% Gd can be obtained. Therefore, Gd-containing DSS has great potential as an ideal neutron absorbing material[25–26]. However, the precipitation behavior and influencing mechanism of element Gd in alloys are obscure, and there are few reports on the unstable transformation of DSS matrix caused by the increase in Gd content and its impact on the mechanical properties of alloys.

This study investigated the influence of Gd on the microstructure and mechanical properties of DSS. The types of the Gd-containing precipitates in DSS and their influence on high-temperature tensile properties of the alloy were also studied.

2 Experiment

The master alloy was 00Cr23Ni8Mo1.4Mn1.4Si0.5 alloy in this experiment. DSS samples with Gd content varying from 0.5wt% to 4.5wt% were fabricated by vacuum induction melting process and used for experiment and analysis. The mass of cast ingot was about 10 kg, and its diameter was 100 mm. The composition of DSS samples was determined by inductively coupled plasma mass spectrometry, and the contents of carbon and oxygen were determined by the carbon sulfur analyzer and oxygen analyzer, respectively. DSS samples with designed Gd content of 0.5wt% , 1.0wt% , 2.0wt%, 3.0wt%, and 4.5wt% are denoted as G0.5, G1, G2, G3, and G4 samples, respectively. The chemical composition of different DSS samples is listed in Table 1. The specific content of Gd added into 00Cr23Ni8Mo1.4Mn1.4Si0.5 alloy is 0.50wt%, 1.05wt%, 2.39wt%, 3.53wt%, and 4.62wt% for G0.5, G1, G2, G3, and G4 samples, respectively. Cylindrical samples with diameter of 8 mm were extracted from the as-cast cylindrical rods by electrical discharge machining.

Table 1 Composition of different DSS samples (wt%)

Sample	Cr	Ni	Mn	Mo	Gd	C	O	Si	Fe
G0.5	23.60	7.70	1.70	1.40	0.50	0.026	0.0030	0.40	Bal.
G1	23.30	8.00	1.60	1.20	1.05	0.023	0.0028	0.40	Bal.
G2	23.70	8.20	1.60	1.20	2.39	0.024	0.0034	0.40	Bal.
G3	23.80	7.70	1.60	1.40	3.53	0.028	0.0016	0.40	Bal.
G4	23.10	8.20	1.70	1.20	4.62	0.024	0.0035	0.40	Bal.

Microstructure was observed by optical microscope (Olympus GX53) and scanning electron microscope (SEM, FEI Quanta 450) after polishing and etching by a modified solution of $K_3Fe(CN)_6$:NaOH:H_2O=1:1:5. The image analysis system was applied to calculate the area percentage of precipitates. Chemical composition and morphology analyses of precipitates were conducted by energy dispersive spectroscope (EDS) and transmission electron microscope (TEM, Tecnai G2 F20), respectively. The thin foils for TEM analysis were prepared by twin-jet electropolishing with a solution of 10vol% perchloric acid and 90vol% aqueous ethanol at −23 ℃ and 19 V.

Nanohardness testing was conducted on a nanoindentation testing machine (TI980) with the sample size of 3 mm in height and 10 mm in cylinder diameter. The load parameter for the test was 30 mN, and the displacement resolution was 10 pm. Each test was measured 3 times, and the data were averaged for further analysis. The hot ductility tests were conducted on Gleeble-1500, and the samples were obtained from cylindrical bars of 60 mm in length and 10 mm in diameter with threaded ends. Before the thermoplastic experiment, the samples were treated with solution at 1100 ℃ for 2 h. The samples were heated to the designed temperature at heating rate of 30 ℃/s and held for 30 s. Then, they were pulled at a cross-head speed of 2 mm/min. Type K-thermocouples were used to monitor the temperature. The section shrinkage of the failed samples was determined as a measure of the hot ductility.

3 Results and Discussion

3.1 Effect of Gd content on as-cast microstructure of DSS

The as-cast microstructures of all samples are depicted in Fig. 1. When the Gd content is 0.5wt%, the microstructure predominantly consists of face-centered cubic austenite and body-centered cubic acicular ferrite with negligible precipitates, as illustrated in Fig. 1a. With the increase in Gd content from 1.05wt% to 3.53wt%, the ratio of the duplex phase markedly alters, resulting in a substantial decrease in austenite content. The second phase is precipitated at the grain boundary and inside the grains, and the morphology of the second phase is mainly elliptical granular, accompanied by a small amount of long strip second phase precipitated at the grain boundary, as shown in Fig. 1b and 1d. In G4 sample, the microstructure is composed of single-phase ferrite, and the austenite structure disappears completely. The

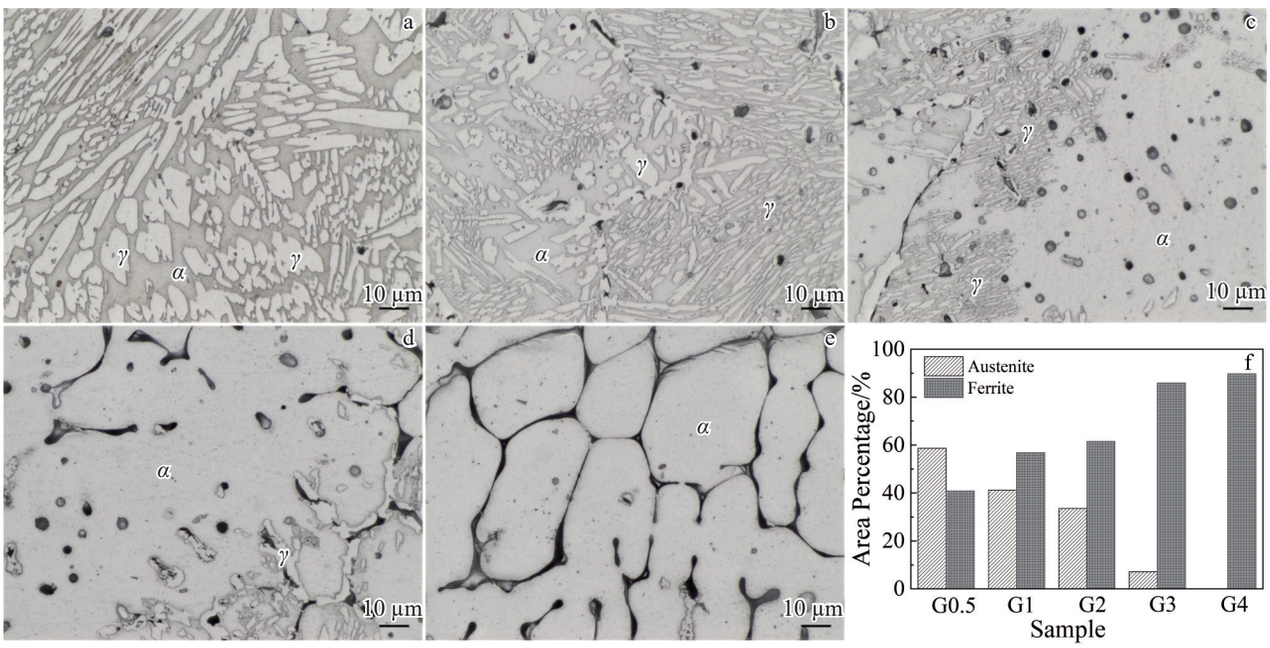

Fig.1 As-cast microstructures of G0.5 (a), G1 (b), G2 (c), G3 (d), and G4 (e) samples; area percentage of ferrite and austenite phases in different samples (f)

second phases are dispersed within a network at the grain boundaries of ferrite, rendering the grain boundaries of the as-cast structure distinctly visible in Fig.1e. Fig.1f illustrates the area percentages, which represent the volume fractions in this case, of ferrite and austenite as a function of Gd content. The area percentage of austenite exceeds that of ferrite in G0.5 sample. In G1 sample, the area percentage of ferrite surpasses that of austenite, and it is progressively increased with the increase in Gd content. In G4 sample, the area percentage of ferrite is nearly 100%.

Fig. 2 illustrates SEM microstructures and area percentage of the second phase in different samples. It can be found that the area percentage of the second phase is increased linearly with the increase in Gd content. The area percentage of the second phase is increased by approximately 2% with every increase of about 1wt% Gd. In G0.5, G1, and G2 samples, the morphologies of the second phase are predominantly manifested as block-like structures. With the increase in Gd content, the morphology of the second phase alters, exhibiting elongated and network shapes, dispersed at the grain

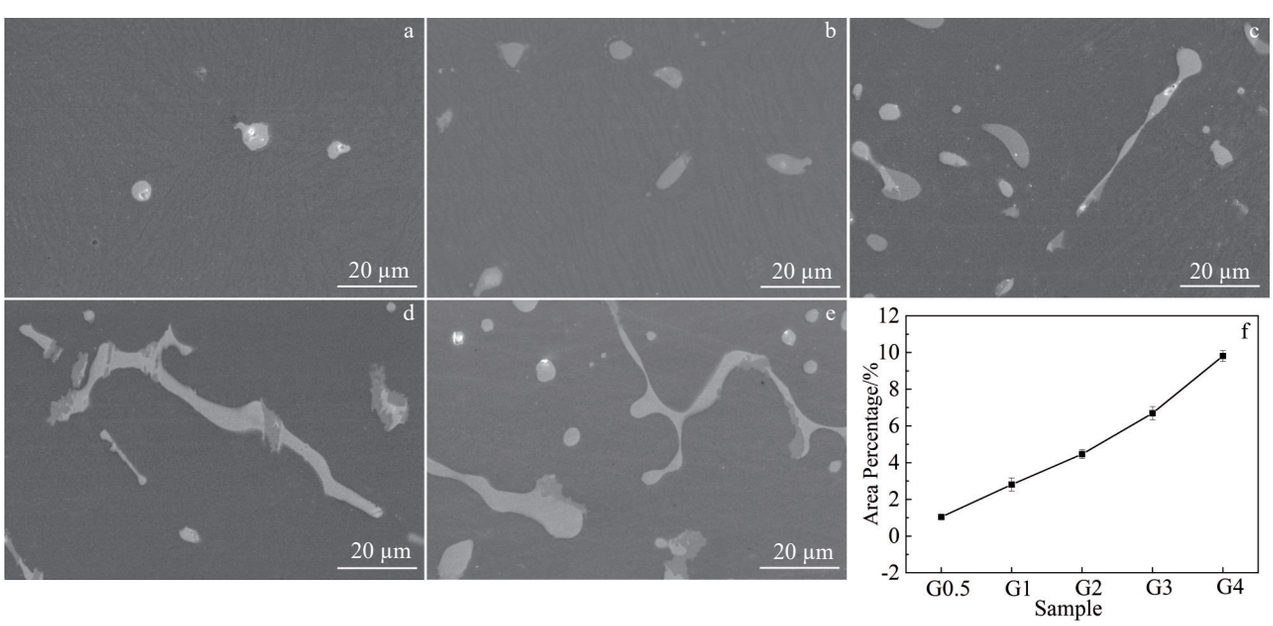

Fig.2 SEM microstructures of the second phase in G0.5 (a), G1 (b), G2 (c), G3 (d), and G4 (e) samples; area percentage of the second phase in different samples (f)

boundaries. Moreover, the higher Gd content results in a larger area of the banded structure.

For further analysis, G2 sample was examined by high-angle annular dark-field scanning transmission electron microscope (HAADF-STEM). Fig. 3 illustrates the existence of two Gd-containing phases in the G2 sample: Gd1 phase and Gd2 phase. Table 2 presents the composition of the Gd-containing phases. It is indicated that Gd1 phase contains Fe, Cr, Ni, and Gd with the content ratio of approximately 48:15:14:19 (wt%), whereas the Gd2 phase consists of Fe, Cr, Ni, and Gd with the content ratio of approximately 18:3:34:43 (wt%). The concentrations of Gd and Ni in the Gd2 phase are approximately double those in the Gd1 phase, whereas the contents of Fe and Cr are significantly lower than those in the Gd1 phase. Moreover, the two Gd-containing phases exhibit an enrichment in Ni and a depletion in Cr, compared to the matrix, which consequently depletes Ni and concentrates Cr in the matrix, thereby influencing the final contents of ferrite and austenite due to the Gd addition. In this case, Gd can be regarded as a ferrite-stabilizing agent that expands the ferrite phase domain. Consequently, an increased Gd content in the alloy results in a larger ferrite content in DSS[14,27].

Fig. 4 illustrates TEM image and corresponding selected area electron diffraction (SAED) patterns of the Gd-containing intermetallic compound, which exhibits a biphasic particle structure. According to Fig. 4b, the lattice parameters are a=0.86 nm and c=0.48 nm for the tetragonal crystal structure. Based on the lattice parameters, chemical composition, and atomic ratio, the Gd1 phase can be identified as the M_{12}Gd phase[17,28]. Fig. 4c indicates that the crystalline structure of the intermetallic compound is in line with that of Ni_3Gd, i.e., a hexagonal phase. The Gd2 phase is identified as the M_3Gd phase, characterized by lattice parameters of a=4.99 nm and c=24.54 nm[17,21].

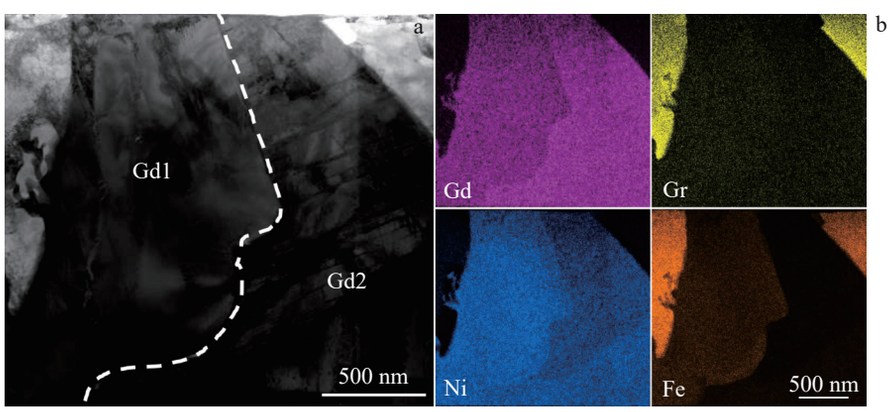

Fig.3 HAADF-STEM image of G2 sample (a) and corresponding EDS element distributions (b) of Gd1 and Gd2 phases

Fig. 5a illustrates SEM image of the randomly distributed aggregated precipitates in G3 sample. EDS results indicate that the composition of the aggregated precipitates is Fe, Cr, Ni, Gd, and O with the content ratio of 5:3:1:23:68 (wt%). Thus, it is inferred that the aggregated oxides are Gd oxide. Most Gd oxide particles are located within the Gd-containing phase with the particle size ranging from approximately 0.5 μm to 5 μm. Despite employing the vacuum smelting technique and incorporating a deoxidizer to diminish oxygen content,

Table 2 Composition of different phases in G2 sample (wt%)

Phase	Fe	Cr	Ni	Gd	Si	Mn	Mo
Austenite	67.80	20.87	9.03	-	0.46	1.84	-
Ferrite	64.38	27.03	5.79	-	0.32	1.57	0.92
Gd1	47.89	15.04	14.28	18.61	1.76	1.42	0.99
Gd2	17.63	3.00	33.84	42.75	1.96	0.82	-

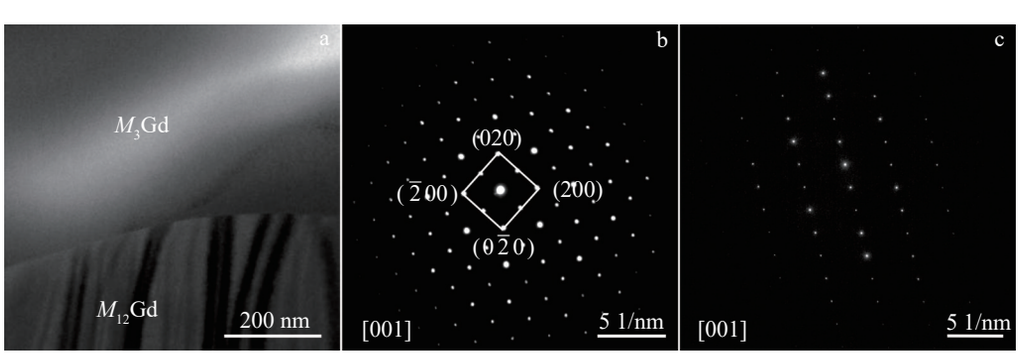

Fig.4 TEM analysis of Gd-containing intermetallic compound: (a) bright-field TEM image of dual-phase compound; (b) SAED pattern of M_{12}Gd phase; (c) SAED pattern of M_3Gd phase

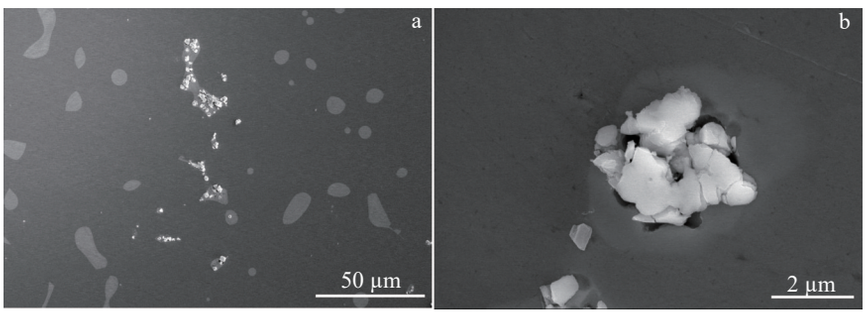

Fig.5 SEM images of G3 sample (a) and Gd oxide (b)

aggregated Gd oxide particles can still be observed in the as-cast samples after the smelting process[24]. This is because among the standard free energies for the formation of Gd-based inclusions, the standard free energy for Gd oxide formation is the smallest: $\Delta G^{\ominus}_{Gd_2O_3}$=−2457 kJ/mol, $\Delta G^{\ominus}_{GdN}$=−760 kJ/mol, and $\Delta G^{\ominus}_{GdS}$=−669 kJ/mol (at 25 ℃, calculated using HSC Thermodynamic program). Consequently, Gd is easily to form Gd oxide.

In summary, as the Gd content increases, the content of Gd-containing DSS alters, resulting in an increase in volume fraction of ferrite and a decrease in volume fraction of austenite. Three phases containing Gd are precipitated in the Gd-containing DSS: M_{12}Gd, M_3Gd, and Gd oxide phases. The WRC-1992 diagram calculations for Ni_{eq} and Cr_{eq} values indicate that the solidification mode of the 00Cr23Ni8Mo1.4-Mn1.4Si0.5 alloy is liquid→ferrite+austenite, and ferrite is the initial precipitate phase[16]. Upon the incorporation of Gd into the alloy, the M_3Gd phase is precipitated via eutectic and peritectic reactions at the solid/liquid interface during solidification, while austenite forms concurrently through the desolventizing transformation of the initially solidified ferrite[29–31]. This phenomenon results in the progressive enrichment of Gd in the liquid phase and facilitates the precipitation of M_{12}Gd and M_3Gd phases. In this case, M_{12}Gd contains 15wt% Ni, and M_3Gd contains approximately 30wt% Ni. Consequently, the formation of the *M*-Gd constituent will significantly deplete Ni and enhance Cr concentration, thereby stabilizing the ferritic matrix. All these factors contribute to the existence of complete ferritic structure in the alloys with elevated Gd concentrations. The Gd content also influences the type of Gd phase. As the Gd content increases, the matrix is transformed from austenite phase to ferrite phase, resulting in the release of excess Ni into the matrix. The M_{12}Gd phase becomes unstable and is progressively transformed into M_3Gd phase, which contains a higher concentration of Ni in the matrix.

3.2 Effect of Gd content on mechanical properties

Fig. 6 shows the room-temperature mechanical properties of G1, G2, and G3 samples. The tensile strength of the samples exhibits a slight increase followed by a slight decrease with the increase in Gd content from 1.05wt% to 3.53wt%, and the maximum tensile strength is approximately 500 MPa (G2 sample). The section shrinkage of the samples is decreased from 2.00% to approximately 0.75% with the increase in Gd content.

Fig. 7 shows the room-temperature tensile fracture microstructures of DSS with different Gd contents, indicating that the tensile fracture mode of all three samples is brittle fracture. According to Fig. 7d–7e, it can be seen that the alloy fracture is characterized by intergranular fracture, which is intrinsically linked to the Gd-containing phase that is precipitated at the grain boundaries. The brittle *M*-Gd precipitates at the grain boundary cannot be co-deformed with the matrix during the hot processing, leading to localized stress concentration. This phenomenon makes the interface between the matrix and the Gd-containing second phase a site for crack initiation, ultimately resulting in fracture under external force[20,32]. The damage to the tensile properties is intensified with the increase in Gd content.

Fig. 8 illustrates the tensile strength and section shrinkage of

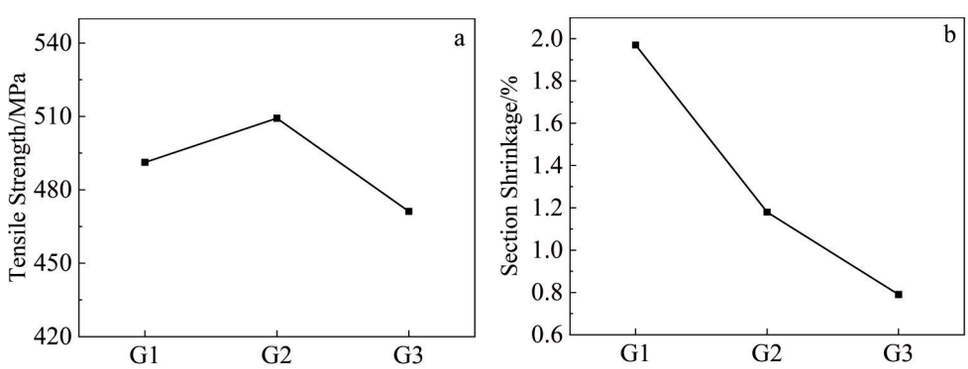

Fig.6 Effect of Gd content on room-temperature mechanical properties of DSS samples: (a) tensile strength and (b) section shrinkage

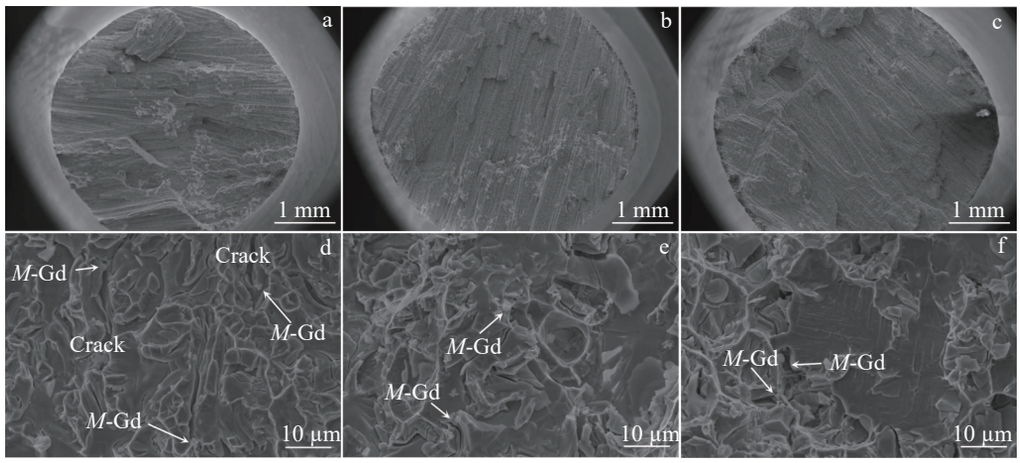

Fig.7 SEM images of room-temperature tensile fracture microstructures of G1 (a, d), G2 (b, e), and G3 (c, f) samples

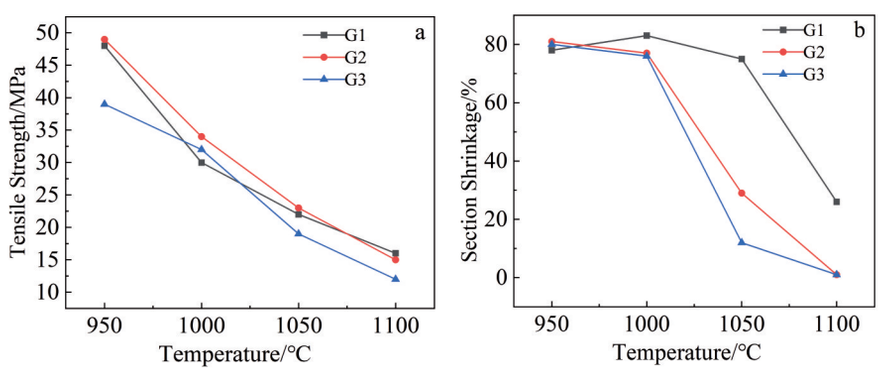

Fig.8 Effect of Gd content on mechanical properties of DSS samples at different temperatures: (a) tensile strength and (b) section shrinkage

G1, G2, and G3 samples at temperatures ranging from 950 ℃ to 1100 ℃. At the same temperature, the tensile strength of G1 and G2 samples is comparable, whereas G3 sample exhibits the lowest tensile strength. With the increase in temperature, the tensile strength of the three alloys is decreased continuously from 50 MPa to about 20 MPa. At 950 ℃, the section shrinkage of G2 and G3 samples is maximum, approaching approximately 80%. When the temperature rises from 1000 ℃ to 1100 ℃, the section shrinkage of the alloys decreases. The overall decrement of section shrinkage is relatively small for G1 sample, and the section shrinkage of G2 and G3 samples is almost 0% at 1100 ℃. The variation trend in section shrinkage performance of DSS samples at high temperatures aligns well with that of 316L stainless steel[14]. For instance, 316L austenitic stainless steel with 1wt% Gd shows a pronounced section shrinkage at 900–950 ℃.

Fig. 9 shows SEM fracture surfaces of G1, G2, and G3 samples at different temperatures. In G1 sample, the tensile fracture is characterized by ductile fracture at 950–1050 ℃; when the tensile temperature is 1100 ℃, the ductile fracture changes to brittle fracture. In G2 and G3 samples, the fracture surface shows ductile fracture characteristic at 950–1000 ℃ and brittle fracture characteristic at 1050–1100 ℃. It can be seen that the increase in both tensile temperature and Gd content will change the fracture behavior of the alloy from ductile fracture to brittle fracture, and the transition temperature is decreased with the increase in Gd content.

Fig. 10 shows SEM fracture surfaces of G1, G2, and G3 samples at different temperatures. At 950 ℃, pronounced necking and numerous dimples can be observed in the fracture microstructure of all three samples. When the Gd content in the alloy increases, at 950 °C, the average diameter and depth of dimples decrease, and the large dimples gradually vanish (Fig. 10a–10c). These phenomena indicate that the increase in Gd content leads to a decrease in toughness of the alloy. At 1100 °C, no dimples are found on the tensile fracture surface, and the oxidation is pronounced. DuPont et al[16] reported that the *M*-Gd phase precipitated at the grain boundaries will melt at 1060 °C. During the high-temperature tension, the melting of the precipitate phase at grain boundary severely weakens the grain boundary bonding, resulting in a sharp decrease in the toughness and plasticity of the alloy.

Fig. 11a–11b show SEM longitudinal sections of fracture surfaces of G2 sample at 950 ℃. Partial Gd oxide appears, leading to agglomeration phenomenon. Under the action of tensile load, Gd oxide cannot co-deform with the matrix, resulting in stress concentration. As the tensile stress increases, the interface fracture between Gd oxide and the matrix results in the debonding of Gd oxide particles and formation of pores.

Fig.11d–11e illustrate SEM longitudinal sections of fracture surfaces of G2 sample at 1100 ℃. It can be found that the

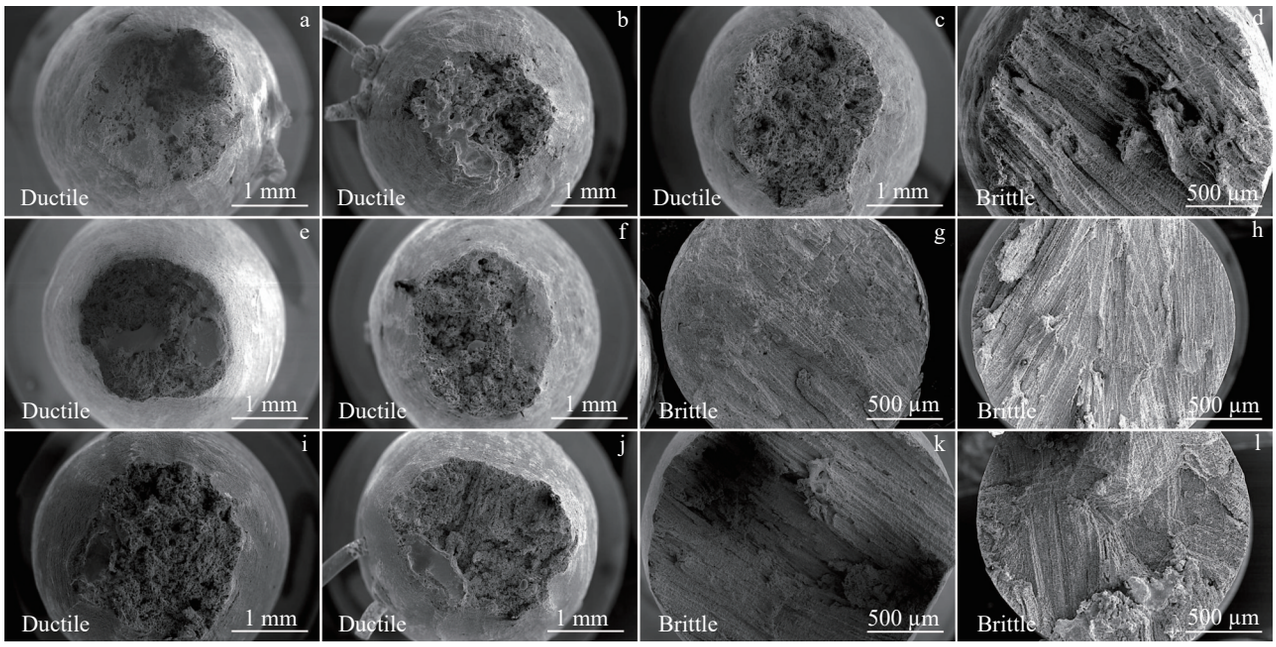

Fig.9 SEM fracture surfaces of G1 (a – d), G2 (e – h), and G3 (i – l) samples at different temperatures: (a, e, i) 950 °C; (b, f, j) 1000 °C; (c, g, k) 1050 °C; (d, h, l) 1100 °C

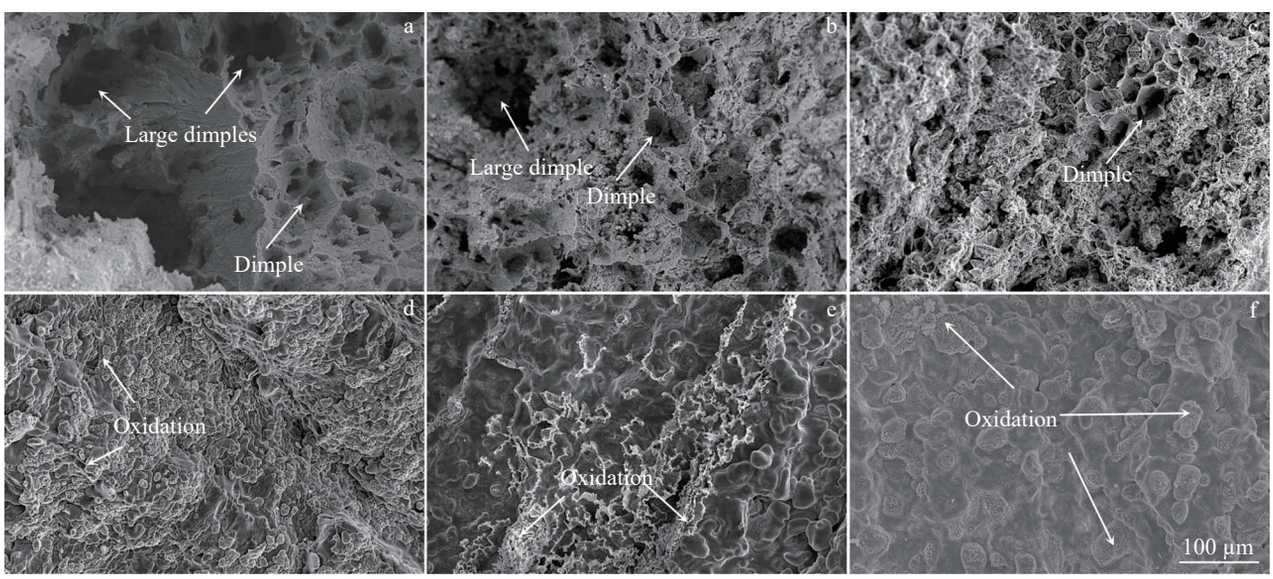

Fig.10 SEM fracture surfaces of G1 (a, d), G2 (b, e), and G3 (c, f) samples at different temperatures: (a–c) 950 °C and (d–f) 1100 °C

fracture occurs at the grain boundary, which is a typical fracture feature along the crystal, but the crack edge is smoother. The oxidized Gd phase and M_3Gd phase are also found at the crack. Combined with the fracture organization (Fig. 11c and 11f), it can be speculated that the M_3Gd phase melts during tension at 1100 °C, resulting in a sharp reduction in grain boundary strength and the plasticity close to 0%. Consequently, it is essential to strictly reduce the oxygen concentration to decrease the Gd oxide content in the alloy during casting, and managing the hot processing temperature is also important to minimize the precipitation of M_3Gd phase.

Fig. 12 illustrates the nanoindentation test results at various locations of G2 sample: austenite matrix, ferrite matrix, M_{12}Gd, and M_3Gd regions. The test was conducted under the maximum load of 30 mN. A more pronounced indentation signifies low hardness of the associated microstructure. The indentation morphology clearly indicates that the two Gd-containing phases possess greater hardness than the matrix.

The nanoindentation hardness and the corresponding elastic modulus at different positions of G2 sample are determined through calculations. The results are presented in Table 3. Notably, the Gd-containing precipitates exhibit a higher hardness but a lower elastic modulus compared to the matrix phases. The elastic modulus of a material serves as a rough

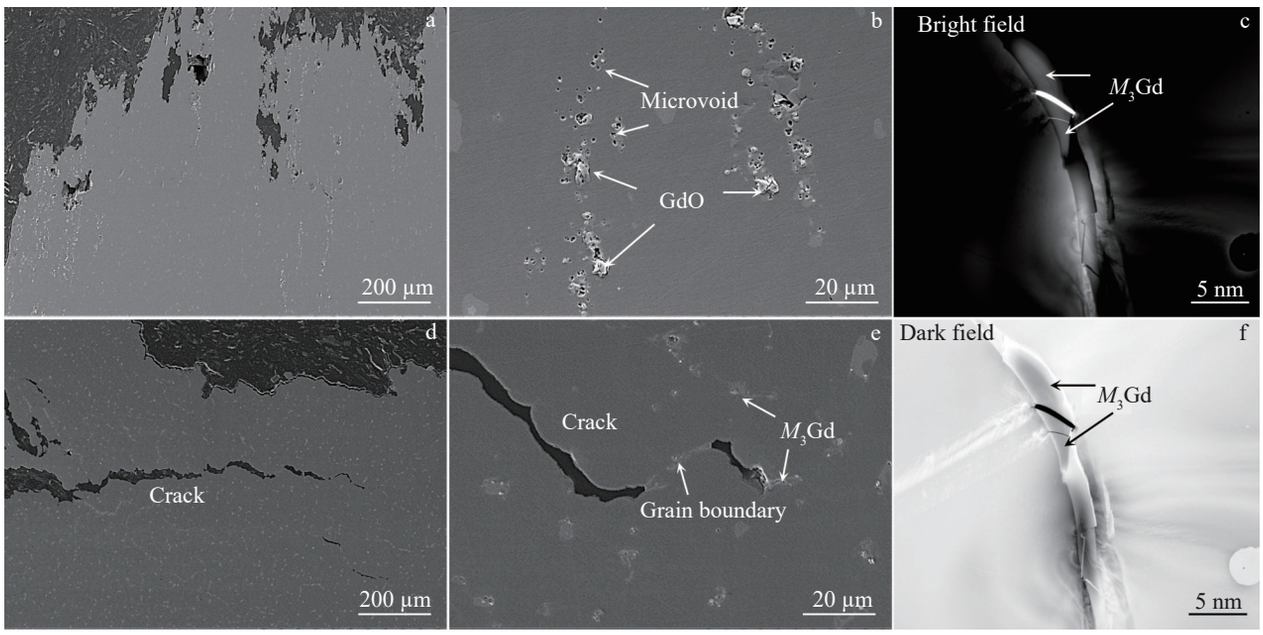

Fig.11 SEM longitudinal sections of fracture surfaces of G2 sample at 950 °C (a–b) and 1100 °C (d–e); HAADF-STEM images of crack location (c, f)

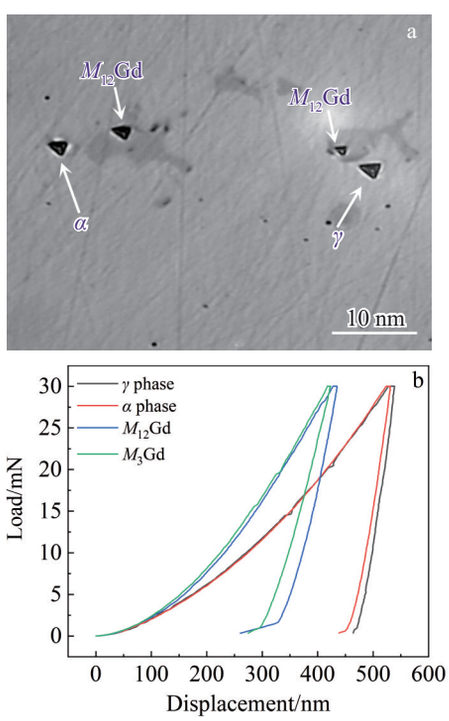

Fig.12 Nanoindentation morphology (a) and load-displacement curves of G2 sample

indicator of its fracture toughness. Generally, a higher elastic modulus correlates with superior fracture toughness[33–36]. This observation suggests that both the Gd-containing precipitate phases are characterized as hard brittle phases, in comparison to those of the matrix, demonstrating a relatively restricted capacity for deformation. M_3Gd displays a significantly higher hardness than M_{12}Gd, implying that M_3Gd imposes a stronger constraint on the mechanical properties of the alloy.

Table 3 Nanoindentation hardness and corresponding elastic modulus at different positions of G2 sample (GPa)

Phase	Hardness	Elastic modulus
Ferrite (α)	3.493	152.836
Austenite (γ)	3.284	188.788
M_{12}Gd	5.231	117.492
M_3Gd	6.615	89.644

Consequently, it is essential to select an appropriate temperature during hot processing to hinder the precipitation of M_3Gd phase.

4 Conclusions

1) With the increase in Gd content, the matrix is transformed from austenite+ferrite to ferrite. Element Gd mainly exists in three forms in the 00Cr23Ni8Mo1.4Mn1.4Si0.5 alloy: Gd_2O_3, M_{12}Gd, and M_3Gd phases.

2) The incorporation of Gd deteriorates the tensile properties of the 00Cr23Ni8Mo1.4Mn1.4Si0.5 alloy. The more the added Gd, the worse the tensile properties of the alloy. This is because the formed hard brittle *M*-Gd phase and Gd oxide phase in the alloy cannot deform in coordination with the matrix and ultimately cause cracking of the alloy. It is imperative to decrease the oxygen content to reduce the Gd oxide content in the alloy during casting to enhance the mechanical characteristics of alloys.

3) The Gd-containing phases (M_3Gd and M_{12}Gd) exhibit higher hardness and lower elastic modulus, in comparison to those of the matrix. The hardness of M_3Gd is significantly higher than that of M_{12}Gd, which means that M_3Gd has a greater destructive effect on the mechanical properties of the alloy. Consequently, it is essential to select an appropriate

temperature during hot processing to hinder the precipitation of M_3Gd phase.

References

1 Chen H S, Wang W X, Nie H H *et al*. *Rare Metal Materials and Engineering*[J], 2020, 49(12): 4358
2 Hong Zhe, Zhao Shangui, Zhang Chunlong *et al. Nuclear Science and Engineering*[J], 2016, 36(3): 411 (in Chinese)
3 Fraser K. *Corrosion*[J], 2013, 69(10): 986
4 Soliman S E, Youchison D L, Baratta A J *et al. Nuclear Technology*[J], 1991, 96(3): 346
5 Dilip J J S, Janaki R G D. *Journal of Materials Engineering and Performance*[J], 2013, 22: 3034
6 Michael K U, Erb K, Aust T. *Scripta Materialia*[J], 2006. 54(6): 1053
7 Karlsson L, Nordén H. *Acta Metallurgica*[J], 1988, 36(1): 13
8 Fu Hanguang. *Foundry Technology*[J], 2006, 27(1): 87 (in Chinese)
9 Cetin M, Ölmez E. *Protection of Metals and Physical Chemistry of Surfaces*[J], 2020, 56: 619
10 Gu Mingfei, Huang Dagui, Zhao Yong *et al. Rare Metal Materials and Engineering*[J], 2022, 51(12): 4726 (in Chinese)
11 Robino C, Mizia R, Dupont J *et al. Packaging, Transport, Storage & Security of Radioactive Material*[J], 2005, 16(1): 49
12 Kang Y R, Lee M W, Kim G N *et al. Nuclear Science and Engineering*[J], 2015, 180(1): 86
13 Khan Z. *Journal of the Southern African Institute of Mining and Metallurgy*[J], 2012, 112(4): 309
14 Robino C V, Michael J R, DuPont J N *et al. Journal of Materials Engineering and Performance*[J], 2003, 12: 206
15 Xie M M, Jia D X, Jia X L *et al. Rare Metal Materials and Engineering*[J], 2025, 54(4): 871
16 DuPont J N, Robino C V, Michael J R *et al. Welding Journal*[J], 2004, 83(11): 289
17 Kang J Y, Jang J H, Kim S D *et al. Journal of Nuclear Materials*[J], 2020, 542: 152462
18 Zhang W, Li C, Su X. *Journal of Phase Equilibria*[J], 1998, 19(1): 56
19 Lo K H, Shek C H, Lai J K L. *Materials Science and Engineering R: Reports*[J], 2009, 65(4–6): 39
20 Zhao Yong, Liu Yunming, Gu Mingfei *et al. Heat Treatment of Metals*[J], 2020, 46(5): 34
21 Pan J, Wang Z X, Mei Q L *et al. Scripta Materialia*[J], 2023, 234: 1359
22 Hu Xiaogang, Du Chengjie, Pan Xiaolong *et al. Materials China*[J], 2024, 43(2): 151 (in Chinese)
23 Choi Y, Moon B M, Sohn D S *et al. Nuclear Engineering and Technology*[J], 2013, 45(5): 689
24 Choi Y, Baik Y, Moon B M *et al. Nuclear Engineering and Technology*[J], 2016, 48(1): 164
25 Lim J, Ahn J H, Moon B M *et al. Journal of Korea Foundry Society*[J], 2015, 35(6): 163
26 Lim J H, Jung H D, Ahn J H *et al. Journal of Korea Foundry Society*[J], 2016, 36(1): 24
27 Baik Y, Kang B K, Choi Y *et al. Nuclear Engineering and Technology*[J], 2021, 53(6): 1887
28 Mooji D B D, Buschow K H J *et al. Journal of the Less Common Metals*[J], 1988, 136(2): 207
29 Baik Y, Choi Y, Moon B M *et al. The Physics of Metals and Metallography*[J], 2015, 116: 1135
30 Ahn J H, Jung H D, Im J H *et al. Materials Science and Engineering A*[J], 2016, 658: 255
31 Wang Shaobing, Zhu Zhu, Sun Wenqiang *et al. Special Steel*[J], 2020, 41(3): 15 (in Chinese)
32 Moon B M, Lee S W, Kim M J *et al. Metals*[J], 2018, 8(7): 474
33 Fischer-Cripps A C. *Surface and Coatings Technology*[J], 2006, 200(14–15): 4153
34 Oliver W C, Pharr G M. *Journal of Materials Research*[J], 2004, 19: 3
35 Cao T S, Bobadilla C, Montmitonnet P *et al. Journal of Materials Processing Technology*[J], 2015, 216: 385
36 Amiri S, Lecis N, Manes A *et al. Mechanics Research Communications*[J], 2014, 58: 10

Gd对中子吸收用双相不锈钢组织和力学性能的影响

贾洞箫[1,2,3]，赵鹏飞[1,2,3]，梁　田[1,2,3]，侯坤磊[1,2,3]，姜岳峰[1,2,3]，马颖澈[1,2,3]

(1. 中国科学院 金属研究所 师昌绪先进材料创新中心，辽宁 沈阳 110016)

(2. 中国科学技术大学 材料科学与工程学院，辽宁 沈阳 110016)

(3. 中国科学院 金属研究所 核用材料与安全评价重点实验室，辽宁 沈阳 110016)

摘　要：研究了不同Gd含量对00Cr23Ni8Mo1.4Mn1.4Si0.5合金显微组织和力学性能的影响。结果表明，Gd元素在合金中主要有3种赋存状态，即Gd_2O_3、M_{12}Gd和M_3Gd相（*M*=Fe， Cr， Ni）。随着Gd含量的增加，含Gd析出相与铁素体相含量增加，而奥氏体相含量降低。氧化钆和2种含Gd相的析出是合金在热变形过程中开裂的主要原因，部分聚集的氧化钆颗粒与晶界上难以变形的含Gd相降低了合金的热延展性。随着Gd添加量的增加，合金的抗拉伸强度和截面收缩率均降低。此外，与M_{12}Gd相比，M_3Gd更为硬脆，对合金的力学性能破坏性更强。

关键词：结构/功能一体化；Gd；双相不锈钢；中子吸收材料；力学性能

作者简介：贾洞箫，男，1997年生，博士，中国科学院金属研究所师昌绪先进材料创新中心，辽宁 沈阳 110016，E-mail：dxjia20s@imr.ac.cn